Geomechanics and Engineering, *Vol. 40, No. 4 (2025) 263-276*
https://doi.org/10.12989/gae.2025.40.4.263

Evaluating the shear strength of anchored jointed rock mass under different normal stiffness conditions

Yang Song*, Jinghan Mao, Heping Wang and Bo Fan

School of Civil Engineering, Liaoning Technical University , Fuxin, Liaoning, 123000, China

(*Received March 12, 2024, Revised February 10, 2025, Accepted February 12, 2025*)

Abstract. This study investigates the constant normal stiffness (CNS) boundary condition in deep rock engineering structures, which provides a more accurate representation of the stress environment of jointed rock masses than the constant normal load (CNL) boundary condition. Three CNS boundary conditions (0 GPa/m, 1.5 GPa/m, and 3.0 GPa/m) were designed to simulate the effects of confinement and various geological engineering conditions on different tunnel depths. Using direct shear tests on both anchored and unanchored joint samples under CNS conditions, this study incorporated the dilation curve of the joints into a model predicting joint shear strength. The model accounts for the effects of CNS boundary conditions, and combines the anchorage resistance model based on the theory of statically determinate beams. It also considers the relationship between axial and lateral displacements of anchors during shear deformation. Results demonstrate that both CNS boundary conditions and anchorage significantly influence shear mechanical properties. Anchor reinforcement exhibited a greater impact on peak shear stress than CNS boundary conditions, while both factors similarly affected peak normal displacement. The newly proposed model accurately predicts shear strength under different normal stiffness boundary conditions, aligning closely with experimental data. The study also analyzes the contribution of anchors to shear strength, revealing a 57.28% contribution under a stiffness condition of 0 GPa/m. With increasing normal stiffness, intrinsic shear resistance in jointed rock mass improves, while the relative contribution from anchors decreases.

Keywords: bolted jointed rock mass; constant normal stiffness; shear dilation curve; shear strength calculation model

1. Introduction

Joints in natural rock masses are influenced by external loads, making them prone to misalignment and slippage, which can lead to rock mass instability and failure. To enhance rock mass stability, bolting technology is widely applied in various rock engineering projects. In tunnel engineering, burial depth significantly affects the stress distribution and deformation patterns of surrounding rock. According to the International Tunneling Association (ITA), a tunnel is classified as deep-buried if the overburden thickness exceeds 50 m or if the burial depth-to-diameter ratio is greater than 20. Although classification criteria vary slightly across countries and regions, the critical burial depth can generally be estimated using the empirical formula Hp=(2~2.5)h0, where Hp represents the critical burial depth and h0 is the overburden thickness after excavation. For instance, the maximum burial depth of the Sichuan–Tibet Railway Tunnel in China reaches 2080 m, making it a typical deep-buried tunnel. In deep-buried tunnel engineering, the high-stress environment poses significant challenges to rock mass stability. Hard rock in deep tunnels is often susceptible to rockbursts, while soft rock may experience severe squeezing deformation of the surrounding rock. These complex geological issues impose stricter stability requirements on deep-buried tunnels. Anchoring technology has been widely adopted to mitigate these effects; rock bolts can effectively control energy release from rockbursts and suppress the plastic deformation of soft rock (Najm and Daraei 2023). However, the stress environment of deep-buried tunnels differs significantly from that of shallow tunnels. Due to the strong confinement of deep surrounding rock, the dilation effect and normal stress distribution of jointed rock masses change considerably, thereby significantly influencing their shear strength. The traditional constant normal load (CNL) boundary condition is typically used to simulate the shear-free deformation behavior of jointed rock masses in shallow tunnels. However, in deep-buried tunnels, where the stress and deformation characteristics of jointed rock masses are more complex, the CNL boundary condition fails to accurately capture their actual behavior. Therefore, a more appropriate boundary condition, such as the constant normal stiffness (CNS) boundary condition, is required to more precisely simulate the shear behavior of jointed rock masses in deep-buried tunnels.

At present, many studies on the joint characteristics of rock bodies have been carried out internationally (Zhang *et al*. 2023, Niktabar *et al*. 2023, Wang *et al*. 2020, Renani *et al*. 2019, Wang *et al*. 2022, Verma *et al*. 2023, Sun *et al*. 2023, Al-E'Bayat *et al*. 2024), and preliminary studies on the shear behavior of jointed rocks under CNS boundary conditions have also been performed. Saadat and Taheri (2020) used PFC2D(Particle Flow Code in 2 Dimensions) software to numerically simulate jointed and unanchored

*Corresponding author, Professor
E-mail: 472220638@stu.lntu.edu.cn

ISSN: 2005-307X (Print), 2092-6219 (Online)

rock bodies with anchored support and explored the importance of constant normal stiffness conditions, surface roughness, concave and convex angles and initial normal stresses. Han *et al*. (2022) experimentally investigated the shear behavior of man-made rock samples containing single or double joints and analyzed and discussed the effects of surface roughness on the evolution of shear stress, normal stress and normal displacement, as well as the damage modes. Usol'tseva *et al.* (2020) conducted straight shear tests on jointed rock bodies made of uniformly structured monolithic sandstone and revealed the deformation and strength characteristics of the jointed rock bodies. The deformation and strength properties of the rock body changed under the influence of the normal load level, boundary conditions and roughness. Wu *et al.* (2022) investigated the importance of the shear expansion behavior of rock joints on the stability of the rock body in deep underground engineering structures and proposed a nonlinear shear expansion model considering the maximum height of undulation, inclination of the bulge, normal stiffness and initial normal stress.

The reinforcing effect of anchor rods on rock has received much attention (Qin *et al.* 2021, Oreste and Spagnoli 2024, Zou and Zhang 2021, Zhu *et al.* 2023, Sarfaraz *et al.* 2021, Kang *et al.* 2023, Srivastava 2023); however, most studies on anchor resistance modeling are based on the boundary condition of constant normal stress. Pellet and Egger (1996) investigated the shear behavior of anchor rods in the nodal surface under lateral constraints and adopted the elastic foundation beam theory; based on the minimum residual energy method established the relationship between the internal force of the anchor rods and the shear deformation, the effects of the anchor rods' anchor angle and diameter, and the strength of the surrounding rock were analyzed. Wang *et al.* (2023) carried out an experimental study on the effect of anchors on the damage and strength behavior of a model of a non-through jointed rock mass and systematically compared and analyzed the strength and damage behavior of a jointed rock mass with/without anchors. He *et al.* (2023) investigated the shear performance of a jointed rock mass anchored by NPR steel, carried out an indoor shear test on bolted rock joints with different normal stresses, and compared and analyzed the strength, deformation, and stability modes of shear; they found that the energy of shear was reduced. The shear strength, deformation and instability of bolted rock joints under different normal stress conditions were analyzed, and the shear energy absorption characteristics were compared. Wu *et al.* (2022) investigated the effect of cyclic shear loading on anchored joints under different joint surface roughnesses through a series of shear tests. Liu and Li (2017) carried out a thorough analysis of the engineering background and scientific significance of research on joint anchoring mechanisms. They investigated the mechanical and deformation evolution patterns of joints under tensile and shear loads and proposed an analytical method based on force equilibrium equations and deformation compatibility relations.

These studies initially revealed the shear mechanical properties and damage characteristics of anchored jointed rock masses under CNS boundary conditions as well as under CNL boundary conditions; they also fully illustrated the mechanical model of anchors under CNL boundary conditions; however, the research and analysis of the shear strength model of the anchored jointed rock masses under CNS boundary conditions are insufficient. To further investigate the mechanical properties and shear strength model of anchored joints under different normal stiffness conditions, this research focuses on the influence of different normal stiffness boundary conditions and anchor reinforcement; the stiffness values of 0 GPa/m, 1.5 GPa/m and 3.0 GPa/m are selected to represent the limitations of the surrounding pressure and other engineering geological conditions on joints under different burial depths of tunneling. Additionally, the influence of the CNS conditions on the dilatancy process of joints is considered, and the theory of static beams is integrated and considered. In addition, the anchor resistance model, which considers the axial and transverse displacement relationship of the anchor shear deformation in joints, adopts an independently designed CNS shear test system to carry out the direct shear tests of jointed rock masses under different normal stiffness boundary conditions; moreover, the influence of anchors and different normal stiffness boundary conditions on the shear behavior of jointed rock and the shear mechanical properties are examined. A model for the shear strength of anchored jointed rock masses under CNS boundary conditions is proposed and provides an important reference for anchoring jointed rock masses in deep tunnels.

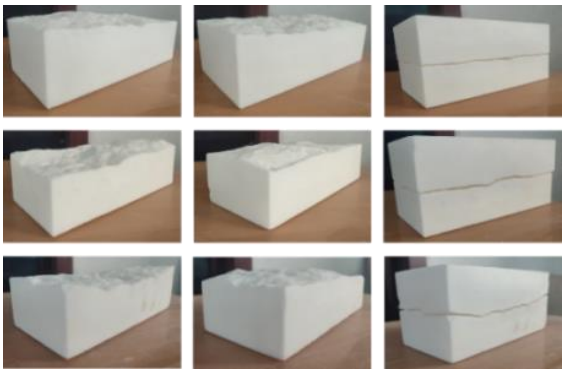

Fig. 1 Schematic diagram of resin film

2. Overview of the experiment

2.1 Specimen preparation

To produce natural joints with a certain roughness, in this study, marble is cut into several rectangular rock blocks with a length, width and height of 200 mm, 100 mm and 100 mm, respectively, according to the size of the shear box. Then, the natural three-dimensional jointing surface data are obtained through a cleavage test, and finally, the cleavage surface is made into a resin mold by 3D printing technology, as shown in Fig. 1.

To accurately assess the magnitude of the roughness of the knuckle surface, a three-dimensional laser scanning

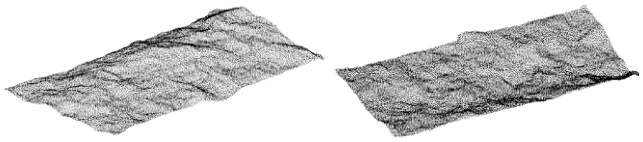

Fig. 2 Schematic diagram of nodal surface scanning

Fig. 3 Schematic Diagram of an Anchored Joint Specimen

Table 1 Basic mechanical parameters of gypsum

Optimum mixing ratio	Hardening time	2 hours expansion rate	24-hour expansion rate	Uniaxial compression strength /MPa
1:0.5	10 min	0.09%	0.13%	12.2

Table 2 Mechanical parameters of the anchors

Ultimate tensile strength /MPa	Tensile yield strength /MPa	Coefficient of elasticity /GPa	Bending ultimate strength /MPa	Ultimate tensile strength /MPa
124	55.2	70	228	124

profiler was used to measure the surface of the cleavage surface, as shown in Fig. 2. According to the 3D scanning data, 50 curves along the shear direction were selected with a spacing of 2 mm, and the roughness of each curve was calculated sequentially by Eqs. (1) and (2). Finally, the average value of the roughness of the 50 selected curves was used as the roughness of the cleavage surface. Tse and Cruden (1979) established the relationship between Z_2 and JRC (joint roughness coefficient)

$$Z_2 = \left[\frac{1}{N} \sum \left(\frac{y_{i-1} - y_i}{x_{i-1} - x_i} \right)^2 \right]^{\frac{1}{2}} \tag{1}$$

$$JRC = 32.2 + 32.47 \cdot \log Z_2 \tag{2}$$

where Z_2 is the root mean square of the slope, N is the number of points on the curve, and x_i and y_i are the coordinates of the points on the curve

Based on the experience from previous researchers, the use of natural rock mass as the test material can more realistically reflect the shear mechanical properties of jointed rock mass but has the clear disadvantage of unreproducible tests. In this study, gypsum was selected as the main material of the test specimen to increase the repeatability and comparability of the test in order to carry out an indoor test. The basic parameters of the gypsum are listed in Table 1.

In the actual project, the row spacing between the anchor reinforcements is usually 3~5 m; because the maximum size of the model specimen is 200 mm and based on the comprehensive consideration of the test conditions, the geometric similarity ratio of the model specimen is 1:20, with 200 mm of the model specimen corresponds to 4 m of the rock mass in the actual project. In addition, the total diameter of the anchor cable is 120 mm; therefore, based on the geometric similarity ratio of the model specimen, a 6061 T5 solid aluminum bar with a diameter of 6 mm is used as the raw material of the anchor rod. The mechanical parameters of the anchor rods are provided in Table 2.

The process of making the specimen is shown below:

(1) The mixing ratio of the materials was determined. According to the optimum mixing ratio of gypsum and the relevant experimental experience, gypsum, water and retarder were weighed at a ratio of 1:0.5:0.005, and the weighed materials were subsequently mixed and thoroughly stirred.

(2) Pouring the upper part of the specimen: First, the sectional resin film was placed into the preprepared mold, the homogeneous gypsum slurry was poured into the mold, and the mold was placed on the vibration table for one minute; this process ensured that the texture of the specimen was uniform and that the gypsum was completely solidified upon removal of the specimen. After, the specimen from the first half of the casting was complete.

(3) Pouring of the lower part of the specimen: The lower half of the specimen was poured according to the pouring sequence in step (2).

(4) Once the specimen has gained sufficient strength after casting, a drilling machine is used to create holes on both the upper and lower joint surfaces. To ensure effective anchoring, the anchor holes must be drilled perpendicular to the specimen's upper and lower surfaces, with a diameter of 8 mm.

(5) Installation of anchor rods: After injecting the anchoring agent—prepared with a mass ratio of gypsum:water:retarder = 1:2:0.005—into the anchor hole, the anchor rod is inserted and stirred up and down to ensure uniform distribution of the anchoring agent and eliminate any voids. The rod is then slowly rotated to align it perpendicularly to the shear direction of the specimen and coaxially with the anchor hole. The anchor rod is a 6 mm diameter solid aluminum bar made of 6061-T5 aluminum alloy.

(6) Specimen maintenance: The completed anchored joint specimens were placed in a dry place to be dried.

The anchored jointed rock mass specimen is shown in Fig. 3.

2.2 Pilot program

In this test, the principle of the control variable method is adopted to analyze the shear mechanical properties of the nodal specimens under the influence factors of normal stiffness boundary conditions, and the test scheme is shown in Table 3. Notably, when the normal stiffness is 0 GPa/m,

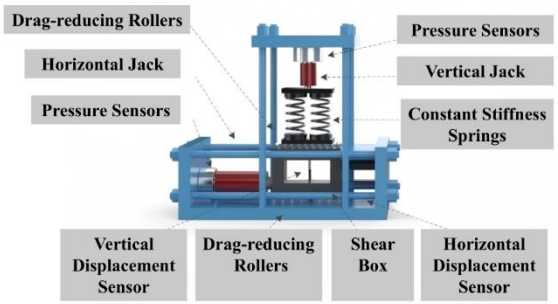

Fig. 4 Schematic diagram of shearing equipment

Table 3 Experimental program

factor	JRC	Initial normal stress /MPa	Normal stiffness /GPa/m	With or without anchor reinforcement
normal stiffness	6.3	0.2	0.0	not have
	6.3	0.2	1.5	not have
	6.3	0.2	3.0	not have
With or without anchor reinforcement	6.3	0.2	0.0	there are
	6.3	0.2	1.5	there are
	6.3	0.2	3.0	there are

the specimen is at the CNL boundary; when the normal stiffness is greater than 0 GPa/m, the specimen is at the CNS boundary.

In this test, an independently designed CNS shear test system was used to carry out the direct shear tests on the nodular rock bodies under CNS boundary conditions.

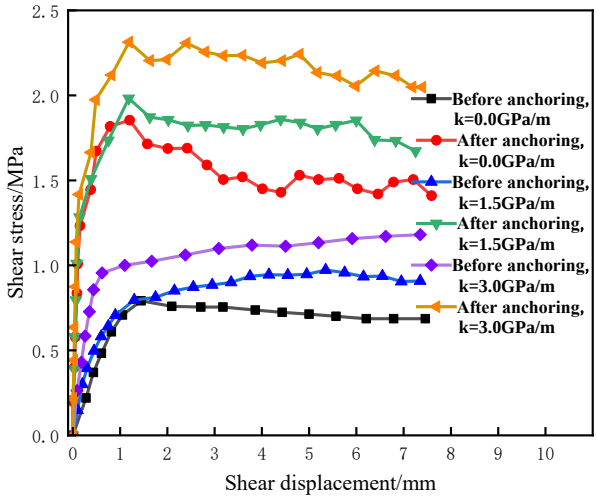

Fig. 5 Shear stress–shear displacement curves of nodal specimens

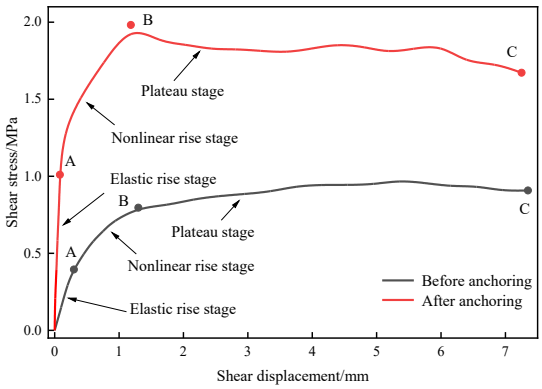

Fig. 6 Characteristic shear stress–shear displacement curves of nodal specimens

3. Test results and analysis

According to the data, the shear stress–shear displacement curves and normal displacement–shear displacement curves before and after anchoring of the nodal specimens under different stiffness values were sequentially plotted, as shown in Figs. 5 and 6, and the characteristic curves of the shear stress and normal displacement were plotted, as shown in Figs. 7 and 8.

3.1 Shear stress–shear displacement curve analysis

Figs. 5 and 6 show that the shear stress–shear displacement curves of the nodal specimens can be divided into three stages: the elastic rise stage, the nonlinear rise stage, and the plateau stage.

(1) In the elastic rise stage, from the comparison of the full-stage shear stress curves of the nodal specimens before and after anchoring, the shear stress curves of the nodal specimens increase the fastest in this stage, and the slopes (shear stiffnesses) of the nodal specimens' shear stress curves differ among the different normal stiffnesses. The shear stiffnesses of the unanchored and anchored nodal specimens increase with increasing normal stiffness, and the shear stiffnesses of the anchored nodal specimens also increase. Specifically, when the normal stiffnesses are 0.0 GPa/m, 1.5 GPa/m, and 3.0 GPa/m, the shear stiffnesses of the unanchored joint specimen are 0.85 GPa/m, 1.51 GPa/m, and 2.08 GPa/m, respectively, and the shear stiffness increases by 77.65% and 37.75%, while the shear stiffnesses of the anchored joint specimen increase by 9.61 GPa/m, 12.38 GPa/m, and 16.02 GPa/m, respectively, and the shear stiffness of the unanchored joint specimen increases by 28.82% and 29.40%, respectively. Compared with those of the unanchored nodal specimen, the shear stiffnesses of the anchored nodal specimens increase by 1031%, 720%, and 670%, and the shear stiffness shows an increase because in normal stiffness condition, the normal stress of the nodal specimen increases as the shear displacement increases; thus the sliding of the joint surface is restricted, and the shear stiffness of the joint surface increases. For the joint specimens reinforced by anchors, the reinforcing effect of anchors restrains the deformation of the joint surface, which enhances the shear stiffness of the joint surface of the jointed rock specimens. Moreover, from the data, the influence of the factor of anchor rods on

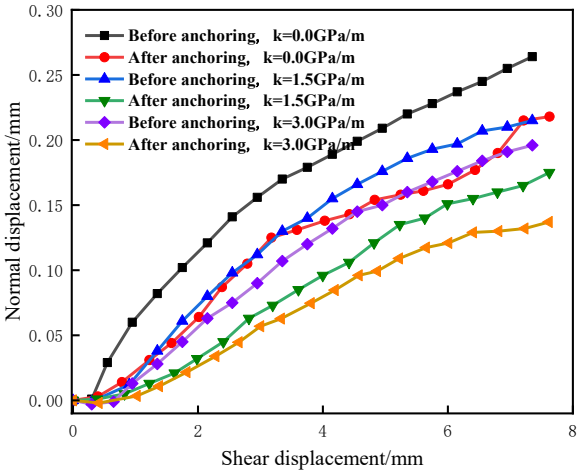

Fig. 7 Normal displacement–shear displacement curve of the nodal specimen

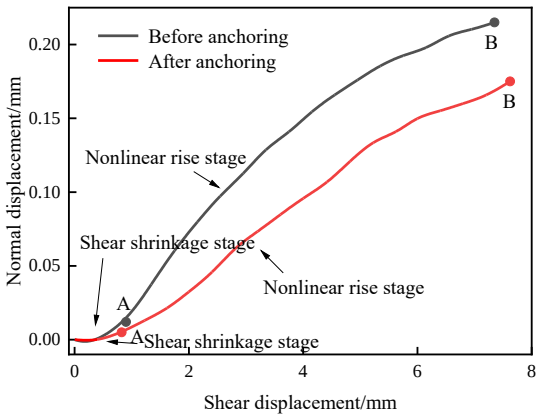

Fig. 8 Characteristic curve of the normal displacement and shear displacement of the nodal specimen

the shear stiffness of joint specimens is much larger than that of the normal stiffness boundary condition.

(2) In the nonlinear rise stage, the rate of increase in the shear stress curve of the nodal specimen begins to decrease, and in this stage, the anchored nodal specimen reaches its peak shear stress. Specifically, when the normal stiffness is 0.0 GPa/m, 1.5 GPa/m, and 3.0 GPa/m, the peak shear stresses of the unanchored nodal specimen are 0.792 MPa, 0.973 MPa, and 1.181 MPa, respectively; the peak shear stresses are increased by 23% and 21%, respectively, and those of the anchored nodal specimen are 1.854 MPa, 1.982 MPa, and 2.313 MPa, with increases of 7% and 17%, respectively. Compared with that of the unanchored joint specimen, the peak shear stress of the anchored joint specimen increased by 134%, 104%, and 96%, and the reasons for the increase in peak shear stress are as follows: in the normal stiffness boundary condition, the increase in the normal stress causes an increase in the shear strength of the joint surface; in the anchored joint specimen, the anchor rods are involved in the shear strength contribution and reach a maximum at this stage. From the data, the contribution of the anchor rods to the nodal shear strength in the anchored nodal specimens occupies a similar weight to the shear strength of the nodal specimens themselves; this is greater than the change due to the increase in the normal stiffness and decreases with the increase in the normal stiffness.

(3) In the plateau stage, the shear stress of the anchored joint specimen decreases after the peak point and reaches the residual strength state because the shear strength of the anchored joint specimen after the generation of the anchor is mainly provided by the joint specimen itself. The unanchored nodal specimen exhibits a stress hardening state under the normal stiffness boundary condition.

3.2 Normal displacement–shear displacement curve analysis

Figs. 7 and 8 show that the normal displacement and shear displacement curves of the nodal specimens can be divided into two phases: the shear shrinkage stage and the nonlinear rise stage.

(1) In the shear shrinkage stage, the joint plane in the jointed specimen is subjected to extrusion, resulting in a gradual decrease in the voids between them, and the degree of closure of the joint plane gradually increases with increasing shear stress.

(2) In the nonlinear rise stage, because of the climbing effect of the rough joints, the shear expansion displacement of the joint specimens begins to increase. Under the same normal stiffness conditions, the normal displacement of the anchored joint specimens significantly decrease, and under different normal stiffness conditions, the normal displacement of the specimens gradually decrease with increasing stiffness. Specifically, when the normal stiffness is 0.0 GPa/m, 1.5 GPa/m, and 3.0 GPa/m, the peak normal displacements of the anchored joint specimens are 0.230 mm, 0.196 mm, and 0.146 mm, which have decreased by 14% and 27%, respectively, and the peak normal displacements of the unanchored joint specimens are 0.264 mm, 0.215 mm, and 0.196 mm, which have decreased by 19% and 10%, respectively, in comparison to those of the unanchored joint specimens. The changes in the displacement are -13%, -9%, and -26%. The decrease in the peak normal displacement occurs because the normal stiffness boundary condition increases the normal stress of the joint specimen, and the normal constraint becomes more evident; this leads to the rough protrusion of the joint surface being partially sheared off, and the normal displacement decreases. Due to the reinforcing effect of the anchors, adding anchors to the joint specimen increases the normal stiffness of the joint surface of the joint specimen; thus, its normal displacement is smaller than that of the unanchored joint specimen.

During the shear process, the joint surface undergoes a transition from the shear contraction stage to the shear dilation stage. In the initial shear contraction stage, the micro-asperities remain in an elastic state and resist shear forces through their inherent strength. At this stage, the normal displacement of the joint surface is primarily attributed to joint closure caused by normal stress. As the shear force increases, the reactive force generated by the elastic micro-asperities can no longer fully counteract the

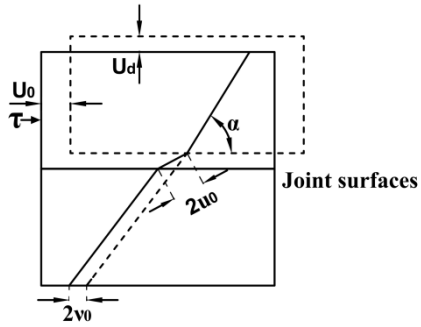

Fig. 9 Schematic diagram of the deformation of the nodal surface

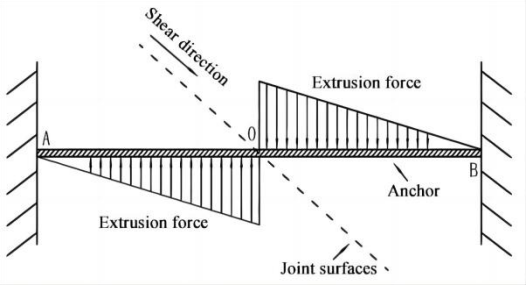

Fig. 10 Model diagram of the super-static beam

applied shear stress. When the shear stress exceeds the basic frictional strength of the micro-asperities, given by $\tau = \sigma_n \tan\varphi_b$, where σ_n is the normal stress and φ_b is the internal friction angle of the rock material, the micro-asperities begin to exhibit a climbing effect. This leads to an increase in the normal displacement of the joints. When the displacement induced by the climbing effect surpasses the closure displacement of the joints, the joint surface transitions into the shear dilation stage.

4. Model for calculating the shear strength of anchored structural surfaces under normal stiffness conditions

4.1 Anchor mechanical modeling

The shear and normal displacements of the joint surface are shown in Fig. 9.

The anchor vs. joint displacement relationship can be deduced from the figure.

$$\begin{cases} v_0 = 0.5\left(U_0 \sin\alpha + U_d \cos\alpha\right) \\ u_0 = 0.5\left(U_0 \cos\alpha + U_d \sin\alpha\right) \end{cases} \tag{3}$$

where U_0 is the horizontal shear displacement of the joint plane, U_d is the normal displacement of the joint plane produced by the shear expansion effect, u_0 and v_0 represent the axial and transverse displacement components of the anchor, respectively, and α is the inclination angle of the anchor (the angle between the axis of the anchor and the nodal plane).

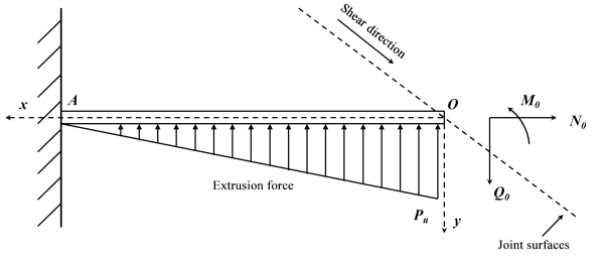

Fig. 11 Static beam model diagram

The deformation of the anchored jointed rock body has a centrosymmetric form with the joint surface as the symmetric surface. When the force of the anchor in the jointed rock mass is analyzed, the anchor can be considered to be a super-static beam. Assuming that the force in the deformed section of the anchor bar is shown in Fig. 10, the anchor bar is regarded as a super-static beam model with fixed beam ends.

The anchors on one side of the nodal face were analyzed, as shown in Fig. 11.

The reaction force distribution of the anchor can be obtained.

$$\begin{cases} P(x) = \dfrac{p_u}{l} \cdot x - p_u \\ p_u = n\sigma_c D \end{cases} \tag{4}$$

where l is the length of the deformed section of the anchor rod, D denotes the bolt diameter (mm), n represents the reaction coefficient (dimensionless), and σ_c signifies the surrounding rock strength (MPa).

Using the microelement segment to analyze the anchor shear, we obtain the following

$$Q(x) = Q_0 - \int_0^x P(x)dx = Q_0 - \frac{P_u}{2l}x^2 + P_u x \tag{5}$$

Since the anchor force is anti-symmetric along the nodal plane, the bending moment of the anchor is zero at point o, and the following equation is obtained

$$M(x) = \int_0^x Q_0 dx = Q_0 x - \frac{P_u}{6l}x^3 + \frac{P_u}{2}x^2 \tag{6}$$

Since the anchor is a straight beam of equal cross-section, the anchor corner equation is defined as follows

$$\varphi = w' = \frac{1}{EI}\left(\frac{Q_0 x^2}{2} - \frac{P_u x^4}{24l} + \frac{P_u x^3}{6} + c_1\right) \tag{7}$$

The deflection equation is defined as follows

$$w = \frac{1}{EI}\left(\frac{Q_0 x^3}{6} - \frac{P_u x^5}{120l} + \frac{P_u x^4}{24} + c_1 x + c_2\right) \tag{8}$$

Substituting the boundary conditions, i.e., the anchor deflection is zero at $x = l$, we obtain c_1 and c_2.

$$\begin{cases} c_1 = -\dfrac{Q_0 l^2}{2} - \dfrac{P_u l^3}{8} \\ c_2 = \dfrac{Q_0 l^3}{3} + \dfrac{11 P_u l^4}{120} \end{cases} \tag{9}$$

Substituting $x = 0$ provides the expression for deflection at the nodal plane of the anchor rod, as follows

$$\begin{cases} \varphi_0 = \dfrac{1}{EI}\left(-\dfrac{Q_0 l^2}{2} - \dfrac{P_u l^3}{8} \right) \\ w_0 = \dfrac{1}{EI}\left(\dfrac{Q_0 l^3}{3} + \dfrac{11 P_u l^4}{120} \right) \end{cases} \tag{10}$$

The axial displacement of the anchor rod is u_0, and the axial displacement of the anchor rod at the nodal surface is caused by the deformation produced by the joint action of the axial force N_0 and the bending moment M, which can be obtained by Hooke's law and the maximum bending moment positive stress formula.

$$u_0 = lN_0 / (EA_m) + M(x)\ l / (EW) \tag{11}$$

where A_m is the cross-sectional area of the anchor and $W = \pi D^3/32$ and is the static moment of the anchor cross-section, which leads to the expression of the relationship u_0 as follows

$$u_0 = \frac{lN_0}{EA_m} + \frac{Q_0 l^2 + \dfrac{p_u l^3}{3}}{EW} \tag{12}$$

Anchor rods will satisfy a certain deformation coordination relationship in the shear process. As shown in Fig. 12, the following assumption are made: O_1 is the position corresponding to point O when only flexural deformation of the anchor rod occurs, O_2 is the position corresponding to point O on the flexural curve, and O_3 is the actual position corresponding to point O after shear deformation of the anchor rod occurs. The length from O to O_3 is defined as u_0, and this length is the axial displacement of the anchor. Additionally, the relevant theory of material mechanics can be obtained from θ as the angle between the straight line where the anchor is located after the flexural deformation at the nodal surface and the straight line where it is located before the deformation; specifically, the angle of turn $\theta = -\varphi_0$, and $\sin\theta = \theta$ applies in the case of the small deformation of the anchor at the elastic stage.

At this point, the following equation can be used

$$a = w_0 \cdot \sin\theta = w_0 \cdot -\phi_0 \tag{13}$$

$$b = u_0 - a = u_0 - \left(w_0 \cdot -\phi_0 \right) \tag{14}$$

The similar triangle relationship is used to find c

$$c = \frac{ab}{w_0} \tag{15}$$

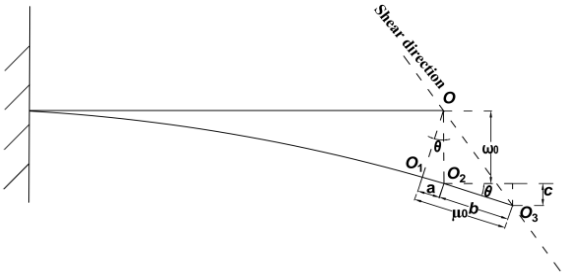

Fig. 12 Schematic diagram of the anchor deformation coordination relationship

Therefore, the lateral displacement of the anchor is as follows

$$v_0 = c + w_0 = -\varphi_0 \cdot u_0 - w_0 \cdot \varphi_0^2 + w_0 \tag{16}$$

Liu and Li (2017) shear test results show that the lateral shear bending section length of the anchor on the structural side is approximately 3~4 times the diameter of the anchor. In this study, to establish a more complete expression of the internal force of the anchor at the structural side, a compromise value is used, i.e., $l = 3.5D$.

$$\begin{cases} u_0 = \dfrac{lN_0}{EA} + \dfrac{Q_0 l^2 + \dfrac{p_u l^3}{3}}{EW} \\ v_0 = -\varphi_0 \cdot u_0 - w_0 \cdot \varphi_0^2 + w_0 \end{cases} \tag{17}$$

From the Pellet and Egger (1996) study, the anchor yielding mode in a jointed rock mass is related to the surrounding rock reaction force Pu, but the other deductions are rather difficult; therefore, in this study, we introduce the yield criterion, the data are substituted, and the value of shear force and axial force are calculated by using MATLAB. Additionally, this value must satisfy the tensile shear yielding equation or bending yielding equation, i.e., Eq. (18) or (19):

$$\sigma_y = \sqrt{\left(\frac{N_{0y}}{A_m} \right)^2 + 3\left(\frac{Q_{0y}}{A_m} \right)^2} \tag{18}$$

where σ_y is the yield stress of the anchor, N_{0y} is the axial force of the anchor at yield, Q_{0y} is the shear force of the anchor at yield, and A_m is the cross-sectional area of the anchor.

$$1.7\sigma_y = \frac{M_A}{W} + \frac{N_{0y}}{A_m} \tag{19}$$

where σ_y is the yield stress of the anchor; M_A is the bending moment at point A of the anchor at yield; $W = \pi D^3/32$ and is the static moment of the anchor section; N_{0y} is the axial force of the anchor at yield; and A_m is the cross-sectional area of the anchor.

4.2 Shear strength modeling of joint rock masses

During the process of joint staggering, the dilatancy effect will occur in the jointed rock mass. Since the external boundary condition is the CNS boundary condition, it will evidently inhibit the dilatancy effect of the jointed rock mass. When the joints after bolt reinforcement are subjected to force deformation, the shear displacement and normal dilatancy of the joints cause the bolt to directly bear part of the shear stress along the joints and produce additional normal stress perpendicular to the joints; this restricts the deformation of the joint plane, greatly increases the nominal stiffness of the joint plane, and plays an evident role in restricting the joint deformation.

According to the study of Wu *et al.* (2022), the shear expansion model of an anchored jointed rock mass under CNS conditions can be expressed as follows

$$\delta_v = \delta_v^p \left(1 - e^{-R_c\left(\delta_h - \delta_h^*\right)}\right) \tag{20}$$

where δ_v is the normal displacement of the nodal specimen, δ_v^p is the peak normal displacement of the nodal specimen, δ_h is the shear displacement of the nodal specimen, δ_h^* is the shear displacement of the nodal specimen when the shear displacement is zero, and R_c is the rate of convergence of the shear expansion.

The following equation is an expression for the shear expansion convergence rate R_c

$$R_c = k\left[1 + d\ln\left(\delta_v^{p^{-1}} \tan i_{ave}\right)\right] \times \left[1 + 6e\left(k_n\right)^f\right] \tag{21}$$

where i_{ave} is the average inclination of the bulge and k, d, e, and f are the rock joint shear expansion convergence rate fitting parameters.

The expression of i_{ave} is as follows

$$i_{ave} = \arctan\left[\frac{1}{(N-1)\Delta x}\sum_{i=1}^{N-1}\left|y_{i+1} - y_i\right|\right] \tag{22}$$

where N is the number of discrete points on the joint curve, Δx is the sampling spacing, and y_i is the height coordinate of the ith point. In this study, the fifty curves selected above are used to calculate the average inclination of the bulge, and finally, the average value is used.

The expression of k_n is as follows

$$k_n = \frac{1}{\frac{1}{k_j} + \frac{1}{k_b}} \tag{23}$$

where k_j is the normal stiffness of the joint face of the anchored joint and k_b is the external normal stiffness.

Due to the coordination of anchor and joint surface deformation, the anchor produces axial deformation, and the internal force generated by this deformation acts on the joint surface as an additional stress, so that the vertical stress on the joint surface changes, changes the stiffness of the joint surface, and produces the effect of interaction between the anchor and the joint surface. At this time, the normal stiffness of the nodal surface of the anchored nodal rock body can be obtained by the following formula

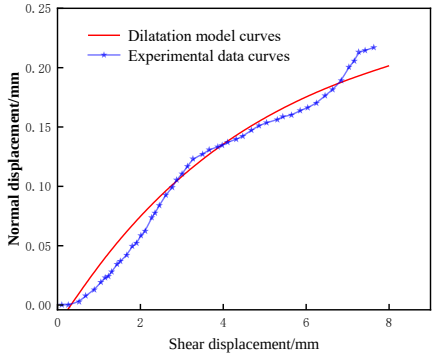

Fig. 13 Comparison of the shear expansion model curves with the test curves

$$k_j = k_j^* + E_b N_b A_m / V_{mc}(1 + 4E_b / 3G_b ctg^2\theta) \tag{24}$$

where k_j^* is the normal stiffness of the nodal surface; E_b, G_b, and A_m are the modulus of elasticity, shear modulus, and cross-sectional area of the anchor, respectively; N_b is the number of anchor rods per unit area of the joint rock mass; V_{mc} is the maximum possible occlusion of the nodal surface; and θ is the inclination angle of the nodal surface.

The equation considers only the shear expansion phase of the shear expansion displacement from 0 to the maximum value and does not consider the initial shear contraction phase of the rock joints. Fig. 13 shows the comparison between the shear expansion model curves and the test curves, and the Pearson correlation analysis of the data using the Origin software yields a Pearson coefficient of 0.9484 and a P value of 9.76564×10^{-5}; thus, the shear expansion model provides a better fit for the shear expansion effect of the nodal surface under the CNS boundary.

Under CNS conditions, the effective normal stress at the nodal surface can be derived from Eq. (25)

$$\sigma_n(h) = \sigma_0 + \frac{k_n \delta_v}{A'} \tag{25}$$

where $\sigma_n(h)$ is the effective normal stress of the joint surface under any shear displacement, σ_0 is the initial normal stress, and A' is the area of the joint surface.

Barton proposed a model for calculating the shear strength of joint surfaces (the JRC-JCS model), but this model did not characterize the shear strength of nodal surfaces under constant normal stiffness boundary conditions; substituting Eq. (24) into this model results in the following model:

$$\begin{cases} \tau_j = \sigma_n(h) \cdot \tan\left\{\varphi_b + (JRC) \cdot \lg\left[\dfrac{JCS}{\sigma_n(h)}\right]\right\} \\ \sigma_n(h) = \sigma_0 + \dfrac{k_n}{A'} \cdot \delta_v^p \left(1 - e^{-R_c\left(\delta_h - \delta_h^*\right)}\right) \end{cases} \tag{26}$$

where τ_j is the shear strength of the nodal surface itself.

4.3 Model for calculating the shear strength of an anchored jointed rock mass

According to Liu and Li (2017), there are four main effects of anchors on the shear strength of joint surfaces:

(1) An increase in axial force of the anchor due to the relative misalignment of the joints and the effect of the axial force relative to the normal component of the joint face on the shear strength of the jointed rock mass.

(2) The effect of the component of the axial force of the anchor parallel to the joint surface on the shear strength of the jointed rock mass.

(3) The anchor rod itself with a certain degree of rigidity, that is, the role of dowel action on the shear strength.

(4) The shear strength of the nodal surface itself.

Combining the above four aspects, we can obtain the specific expression for the shear strength τ of the rock mass with anchored joints

$$\begin{cases} \tau = \tau_{ba} + \tau_{bt} + \tau_j \\ \tau_{ba} = \dfrac{N_0}{A} \cdot \left(\sin\alpha \cdot \tan\varphi_b + \cos\alpha\right) \\ \tau_{bt} = \dfrac{Q_0}{A} \cdot \left(\sin\alpha - \tan\varphi_b \cdot \cos\alpha\right) \\ \tau_j = \sigma_n(h) \cdot \left\{ \varphi_b + (JRC) \cdot \lg\left[\dfrac{JCS}{\sigma_n(h)}\right] \right\} \end{cases} \tag{27}$$

where τ_{ba} is the shear strength converted to the axial force of the anchor in the shear process and τ_{bt} is the shear strength converted to the transverse shear force of the anchor in the shear process.

In summary, we can calculate the shear strength of an anchored jointed rock mass under CNS boundary conditions as follows:

(1) Given the initial shear nodal displacement, the corresponding axial and transverse deformations of the anchor are calculated by Eq. (3).

(2) The anchor shear and axial forces are calculated from the axial and lateral deformation equations of the anchor obtained from the mechanical model, as shown in Eq. (17).

(3) Determination of whether the anchor shear axial force satisfies the tensile shear yielding equation or bending yielding equation is accomplished through Eqs. (18) and (19).

(4) The initial shear nodal displacement is increased if the yield equation is not satisfied. The above steps are repeated until the anchor axial shear force satisfies the tensile yield equation.

(5) The shear strength of the nodal rock mass under constant normal stiffness conditions is obtained by substituting the anchor axial force and shear force into Eq. (27).

5. Model Validation and analysis

5.1 Validation of the model

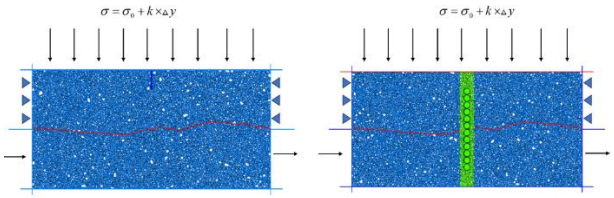

Fig. 14 numerical model

Table 4 PFC mesoscopic parameters

parameter	Valid values
Minimum radius/mm	0.35
Maximum radius/mm	0.5
Porosity	0.14
Coefficient of friction	0.3
Modulus of elasticity/GPa	3.5
Stiffness ratio	1.0
Parallel bonding effective modulus of elasticity/GPa	3.5
Parallel bond stiffness ratio	1.5
Cohesion within parallel bonding/MPa	3.0
Tensile strength of parallel bonding/MPa	6.0
Parallel bonding friction angle/°	0.0
Normal stiffness/GPa	100
Tangential stiffness/GPa	50
Coefficient of friction	0.84

To accurately simulate the discrete contact and inter-particle mechanical behavior of the joint surface, numerical simulations were conducted using the particle flow software PFC2D to validate the experimental and theoretical results. The numerical model has a size of 200 mm and consists of an upper and lower rock mass with a joint surface in between. The rock matrix was modeled using the parallel bond model, while the joint surface was predefined by importing its surface profile and modifying the contact model of particles near the joint surface to a smooth-joint model. In the anchoring model, anchor particles were represented as rigid cluster units with a radius of 3 mm, with a total of 12 anchor particles included in the simulation. The specific numerical model is shown in Fig. 14.

In PFC2D software, the determination of mesoscopic parameters for the model is critical. Ensuring result accuracy necessitates repeated trial-and-error iterations. Therefore, this study calibrates the meso-mechanical parameters of the numerical model by comparing stress-strain curves from uniaxial compression tests and numerical simulations. Furthermore, laboratory shear test results are employed as a reference to iteratively adjust the mesoscopic parameters of rock particles, grout particles, and bolt particles within the numerical model. A schematic comparison between uniaxial compression tests and numerical simulations is illustrated in Fig. 15, while Fig. 16 presents a comparative analysis of numerical simulations

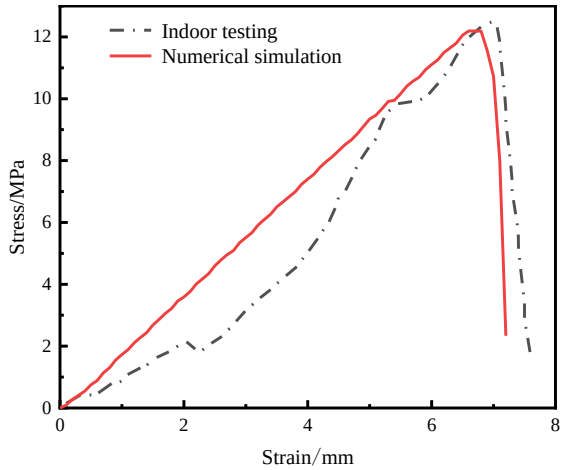

Fig. 15 Schematic comparison between uniaxial compression tests and numerical simulations

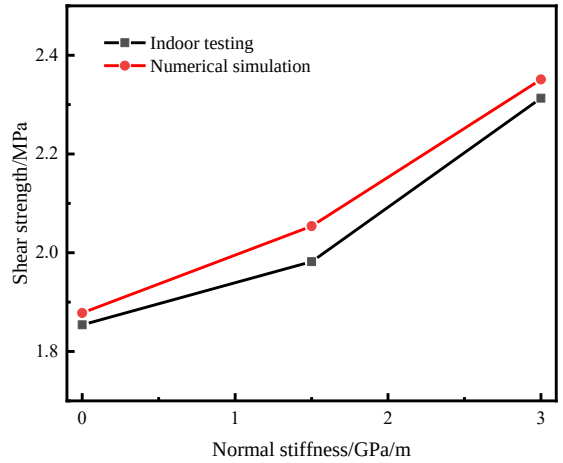

Fig. 16 Comparison between numerical simulations and laboratory tests

and laboratory tests. The results demonstrate that the numerical simulations closely align with experimental outcomes, indicating that the mesoscopic parameters of the numerical model effectively capture the mechanical behavior of the specimen. The specific mesoscopic parameters of the numerical model are listed in Table 4.

According to the expression for the shear strength of the anchored jointed rock body derived in this study, to calculate the shear strength of the specimen, the uniaxial compressive strength and the angle of internal friction of the jointed specimen needs to also be determined. A uniaxial compression test of the gypsum material was carried out, and the uniaxial compressive strength of the joint face wall was 12.2 MPa. According to Fig. 17, the corresponding reaction coefficient of the gypsum specimen is 9.2.

The specimens used in this test were unfilled nodular specimens; thus, the internal friction angle of the nodular specimens was determined only by the roughness of the nodular surface. Han (2019) defined the maximum undulation inclination of the nodal surface contour lines along the shear direction as the critical undulation inclination, and the specific operation for obtaining the

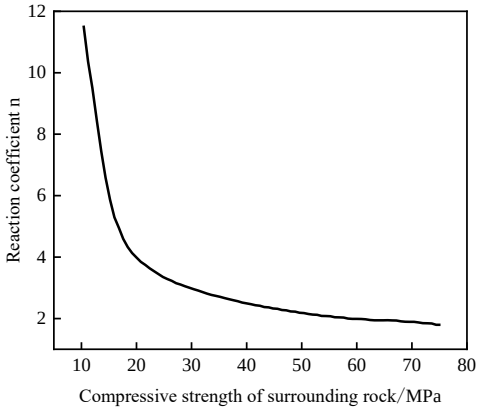

Fig. 17 Values of n for different compressive strengths of the surrounding rock

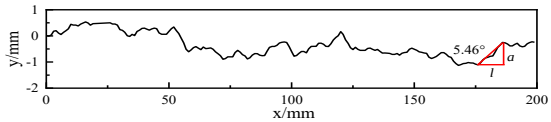

Fig. 18 Critical large undulation inclination for roughness knots

critical undulation inclination was as follows: first, 50 curves along the shear direction were selected as the contour lines with a spacing of 2 mm; second, the maximum undulation inclinations from 50 contour lines were separately calculated; and finally, the average value of the 50 undulation inclinations was used as the critical undulation inclination, which was calculated by the following formula: . Finally, the average value of these 50 maximum heave inclinations was used as the critical large heave inclination, which was calculated by the formula $\alpha = \arctan(a/l)$. The results showed that a larger critical major undulation inclination correlated to a rougher joint surface, and a larger shear displacement is generated in the shear process; thus, the critical major undulation inclination of the joint surface can better characterize the roughness of the joint surface. Therefore, based on the results from Han Guansheng's study, the internal friction angle of the joint surface can be approximately equal to the key major undulation inclination of the joint surface in our study. As shown in Fig. 18, the internal friction angle of the nodular specimen in this study is 5.46°.

In summary, the fundamental mechanical parameters of the aforementioned anchored joint specimens can be incorporated into the mechanical model calculations to determine the axial and shear forces. By substituting these shear and axial forces, the shear strength of the anchored joint specimens under constant normal stiffness boundary conditions can be derived. A comparative analysis of the theoretical predictions, laboratory test results, and numerical simulation values is systematically presented in Table 5.

As shown in Table 4, a certain deviation is observed between the theoretically calculated values and the laboratory test values derived from the analytical model of the shear strength of the rock mass with anchored joints

Table 5 Comparison of the theoretical calculated values and indoor test values

factor	Shear strength/MPa				
	experimental value	theoretical value	Relative error/%	numerical simulation value	Relative error/%
k=0.0 GPa/m	1.854	2.018	8.84	1.878	6.04
k=1.5 GPa/m	1.982	2.097	5.81	2.054	2.06
k=3.0 GPa/m	2.313	2.534	9.56	2.351	7.22

Table 6 Scale Effect Data Summary Table

Size/mm	Shear strength/MPa		
	Normal stiffness/GPa/m		
	0	1.5	3
200	0.811	0.987	1.204
400	0.625	0.722	0.991
600	0.525	0.601	0.801
800	0.466	0.511	0.601
1000	0.421	0.431	0.491

investigated in this study; however, the relative error is within the acceptable range.

5.2 Scale effect analysis

The investigation of scale effects in rock mass mechanics has long been a critical research focus. To explore the influence of scale effects on the shear strength of jointed rock masses, this study employs PFC2D software for numerical simulations, constructing rock mass models with varying dimensions. By simulating models of different sizes, the study systematically examines the scaling laws governing the shear strength of jointed rock masses. Under controlled roughness conditions, a dimensional series of 200, 400, 600, 800, and 1000 mm is adopted to investigate shear strength variations under distinct normal stiffness boundary conditions. Detailed simulation data are summarized in the table..

Based on the data presented in the table, the scale effect diagrams of peak shear stress under different normal stiffness conditions were generated. As illustrated in the figures, the shear strength of jointed rock masses exhibits a nonlinear decrease with increasing specimen size, which conforms to a power-law function expressed as

$$\tau = m \cdot s^{n} \tag{28}$$

where m and n are empirical coefficients, and s represents the specimen size.

The analysis reveals that the parameters m and n in the scale effect function vary significantly with normal stiffness (kn). Through nonlinear regression, the following relationships were established: m=4.4798*kn+7.2555, b=-0.0398*kn+-0.4185.

Substituting these expressions into the original power-law function yields a normal stiffness-dependent size effect

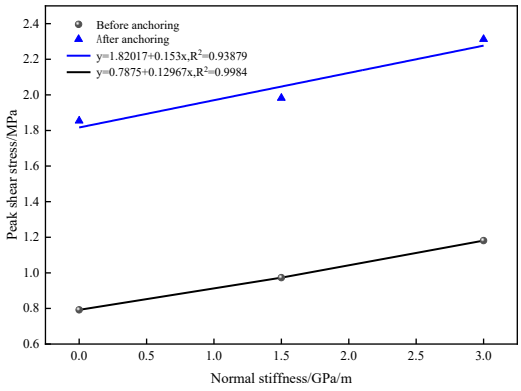

Fig. 19 Fitted curves of the peak shear stress before and after anchoring of the nodal specimens with different normal stiffnesses

relationship for shear strength

$$\tau = (4.4798 \cdot k_n + 7.2555) \cdot s^{-0.0398 \cdot k_n + -0.4185} \tag{29}$$

5.3 Strength Analysis of the Anchor Resistance Contributions

Building upon existing research and the derivations from Eqs. (17) and (24) in the preceding section, increasing the bolt diameter D_b modulates the calculation of the deformation segment length of the rock bolt. This adjustment amplifies the shear resistance contributions of the bolt to the joint interface (τ_{ba} and τ_{bt}), thereby enhancing the bolt's mechanical efficacy. However, as long as the anchor length exceeds the deformation length near the joint surface, further increasing its length has minimal impact on the reinforcement effect. In practical anchoring engineering, optimizing bolt diameter within feasible limits is an effective reinforcement strategy. However, due to manufacturing constraints and construction equipment limitations, commercially available rock bolts adhere to standardized specifications, necessitating diameter adjustments within a finite range to maximize reinforcement benefits.

This study employs fully grouted rock bolts with fixed dimensions to evaluate anchoring effects by analyzing pre- and post-anchoring shear strength variations in jointed specimens. To quantitatively assess the shear strength enhancement under varying normal stiffness conditions, comparative analyses were conducted between the fitted curves of peak shear stress for anchored and unanchored joint specimens, as illustrated in Fig. 19. The results demonstrate that both fitted curves exhibit a linearly increasing trend with rising normal stiffness.

In addition, the peak shear stress of the anchored joint specimens was significantly greater than that of the unanchored joint specimens; these results indicated that the strength of the anchor bars contributed a large proportion of the shear strength of the specimens during the shear process. To further analyze the anchoring effect of the

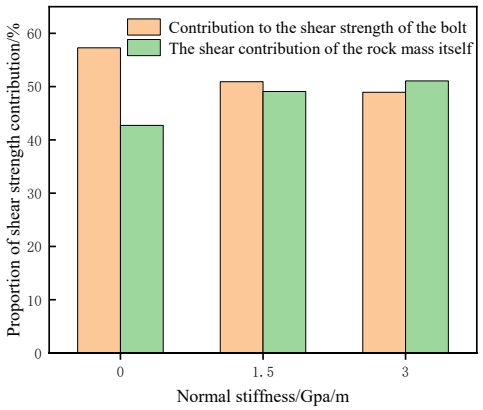

Fig. 20 Percentage of the strength contributed by anchors

Table 7 Peak shear stresses of the nodal specimens before and after anchoring under different normal stiffness conditions

Normal stiffness/(GPa/m)	Peak shear stress/MPa		Anchor contributing strength/MPa
	pre-anchorage	post-anchorage	
0.0	0.792	1.854	1.062
1.5	0.973	1.982	1.009
3.0	1.181	2.313	1.132

anchor rods, the peak shear stresses are compiled before and after anchoring of the three groups of joint specimens with normal stiffnesses of 0.0 GPa/m, 1.5 GPa/m, and 3.0 GPa/m, and the difference between the peak shear stresses before and after anchoring of the specimens is defined as the contributing strength of the anchor rods, which is provided in Table 7.

Table 5 shows that the contributing strength of the anchors tends to increase with increasing normal stiffness. When the normal stiffness is 0.0 GPa/m, 1.5 GPa/m, and 3.0 GPa/m, the contributing strengths of the anchor rods are 1.062 MPa, 1.009 MPa, and 1.132 MPa, respectively.

According to the derivation of this study, the shear strength of the anchored joints can be divided into the shear strength of the joints themselves and the strength contributed by the anchor rods; from these results, the proportions of the strength contributed by the anchor rods are calculated to be 57.28%, 50.91%, and 48.94% when the normal stiffness is 0.0 GPa/m, 1.5 GPa/m, and 3.0 GPa/m, respectively. These results indicate that the proportion of the total shear strength accounted for by the anchors decreases; specifically, the anchoring effect decreases as the normal stiffness increases. Thus, with increasing normal stiffness, the contribution strength of the anchor also increases; however, the proportion of the total shear strength accounted for by the strength contribution from the anchor decreases, where the anchoring effect of the anchor decreases. The above phenomenon occurs because with increasing normal stiffness in the shear process, the specimen is subjected to greater normal stress; this greater stress of the specimen on the upper and lower joint surface is shown by an increase in the shear strength of the joint rock mass. Moreover, above trend is greater than the trend of the anchor's contribution to the strength, which agrees with the formula deduced in this study; specifically, the anchor rod not only shares the external force but also increases the normal stiffness of the joint surface, k_j remains unchanged, and the normal stiffness boundary condition k_b increases, resulting in an increase in the influence exerted on the joint specimen.

6. Conclusions

To study the shear strength of anchored jointed rock masses under different normal stiffness conditions, shear tests were conducted on jointed rock mass specimens to establish a shear strength model of anchored jointed rock masses under CNS conditions, and the following conclusions are obtained:

(1) The CNS boundary condition and anchor reinforcement significantly influence the shear mechanical properties of jointed specimens. Under the CNS boundary condition, the normal stress on the jointed specimen increases as shear progresses, leading to changes in shear stiffness and normal stiffness. As a result, the first-stage shear stiffness and peak shear stress increase, while the peak normal displacement decreases. The anchoring effect of rock bolts can be summarized in two key aspects: first, the anchor shares part of the external load, enhancing the shear resistance of the jointed specimen; second, it reinforces the joint surface, constraining its deformation and effectively increasing its nominal stiffness. This, in turn, leads to higher peak shear stress and reduced peak normal displacement. Compared to unreinforced specimens, the contribution of anchor reinforcement to shear stiffness and peak shear stress is more significant than the effect of normal stiffness on the jointed specimen. However, in terms of normal displacement, both exhibit similar trends. This indicates that the combination of anchor reinforcement and the CNS boundary condition plays a crucial role in enhancing the shear strength of jointed rock masses.

(2) Based on the statically determinate beam theory and the relationship between the axial and lateral displacements of the anchor during shear deformation, an anchor resistance model was developed. Additionally, by considering the dilation behavior of jointed rock masses under CNS conditions, a shear strength model for jointed rock masses was established. By integrating these two models, a new shear strength model for anchored jointed rock masses was derived. Comparisons between the model's predictions, direct shear test results, and numerical simulations indicate that the proposed model closely aligns with experimental findings, effectively predicting the shear strength of anchored jointed rock masses under different normal stiffness boundary conditions. Furthermore, it was observed that as the rock mass size increases, its shear strength follows a power-law decay. A scale effect function relating shear strength to normal stiffness was also derived, providing valuable guidance for the design of rock mass anchoring engineering.

(3) In the shearing process of the joint specimen, the strength contribution of the anchor bar contributes a large proportion of the shear strength of the specimen. At a normal stiffness of 0.0 GPa/m, the strength contribution proportion of the anchor bar is 57.28%. As the normal stiffness increases, the strength contribution proportion of the anchor bar to the total shear strength decreases even though the strength contribution from the anchor bar increases; specifically, the trend of the joint itself is greater than the increasing trend of the strength contribution of the anchor bar, and the strength contribution of the anchor bar decreases. The anchoring effect of the anchor has a decreasing trend; this is shown in the shear model as k_j (the normal stiffness of the nodal surface of the nodal rock after anchoring) remains unchanged, and the normal stiffness boundary condition k_b increases, which causes an increase the influence exerted on the nodal specimen.

Acknowledgments

The research described in this paper was financially supported by the National Natural Science Foundation of China (51974146, 52174078) and the Liaoning Provincial Innovative Talent Support Program for Colleges and Universities (21-1071).

References

Al-E'Bayat, M., Guner, D., Sherizadeh, T. and Asadizadeh, M. (2024), "Numerical investigation for the effect of joint persistence on rock slope stability using a lattice spring-based synthetic rock mass model", *Sustainability*, **16**(2), 894. https://doi.org/10.3390/su16020894.

Han, G. (2019), " Study on the shear mechanical properties of rock jointed structures under constant normal stiffness", Ph.D. Dissertation, China University of Mining and Technology, Xuzhou.

Han, G., Zhou, Y., Liu, R., Tang, Q., Wang, X. and Song, L. (2022), "Influence of surface roughness on shear behaviors of rock joints under constant normal load and stiffness boundary conditions", *Nat. Hazards*, **112**(1), 1-19. https://doi.org/10.1007/s11069-021-05185-8.

He, M., Ren, S., Xu, H., Luo, S., Tao, Z. and Zhu, C. (2023), "Experimental study on the shear performance of quasi-npr steel bolted rock joints", *J. Rock Mech. Geotech.*, **15**(2), 350-362. https://doi.org/10.1016/j.jrmge.2022.03.011.

Kang, Y., Hou, C., Xu, C., Liu, B. and Xiao, J. (2023), "Investigation on mechanical behavior of pre-tensioned bolt in fractured rock mass using continuum discontinuum element method(cdem)", *Eng. Anal. Bound. Elem.*, **151**, 30-40. https://doi.org/10.1016/j.enganabound.2023.02.056.

Liu, C.H. and Li, Y.Z. (2017), "Analytical study of the mechanical behavior of fully grouted bolts in bedding rock slopes", *Rock Mech. Rock Eng.*, **50**(9), 2413-2423. https://doi.org/10.1007/s00603-017-1244-9.

Najm, S.J. and Daraei, A. (2023), "Forecasting and controlling two main failure mechanisms in the Middle East's longest highway tunnel", *Eng. Fail. Anal.*, **146**, 107091. https://doi.org/10.1016/j.engfailanal.2023.107091.

Niktabar, N.S.M., Rao, K.S., Shrivastava, A.K. and Ščučka, J. (2023), "Effect of varying normal stiffness on soft rock joints under cyclic shear loads", *Materials (Basel, Switzerland)*, **16**(12), 4272. https://doi.org/10.3390/ma16124272.

Oreste, P. and Spagnoli, G. (2024), "Two-dimensional numerical analysis on the rock/bolt interaction considering shear and normal relative displacements", *Tunn. Undergr. SP. Tech.*, **143**, https://doi.org/10.1016/j.tust.2023.105492.

Pellet, F. and Egger, P. (1996), "Analytical model for the mechanical behaviour of bolted rock joints subjected to shearing", *Rock Mech Rock Engng*, **29**, 73-97. https://doi.org/10.1007/BF01079755.

Qin, S., Wu, K. and Shao, Z. (2021), "Analytical assessment of coupled influences of surrounding rock reinforcement and deformation release on tunnel response", *Geomech. Eng.*, **26**(6), 541-550. https://doi.org/10.12989/gae.2021.26.6.541.

Renani, H.R., Martin, C.D. and Cai, M. (2019), "An analytical model for strength of jointed rock masses", *Tunn. Undergr. Sp. Tech.*, **94**, 103159-103159. https://doi.org/10.1016/j.tust.2019.103159.

Saadat, M. and Taheri, A. (2020), "A numerical study to investigate the influence of surface roughness and boundary condition on the shear behaviour of rock joints", *Bull. Eng. Geol. Environ.*, **79**(prepublish), 1-16. https://doi.org/10.1007/s10064-019-01710-z.

Sarfaraz, V., Asgari, K. and Nasrollahi, M. (2021), "Interaction between rock bolt and rock bridge under tensile loading ", *Geomech. Eng.*, **25**(6), 455-471. https://doi.org/10.12989/gae.2021.25.6.455.

Srivastava, L.P. (2023), "Strength prediction of a passive bolt-reinforced natural jointed rock under confined condition", *Innov. Infrastruct. Solut.*, **8**(5), https://doi.org/10.1007/s41062-023-01117-6

Sun, B., Yang, P., Luo, Y., Deng, B. and Zeng, S. (2023), "Damage constitutive model of jointed rock mass considering structural features and load effect", *Rev. Adv. Mater. Sci.*, **62**(1), https://doi.org/10.1515/rams-2023-0129.

Tse, R. and Cruden, D. (1979), "Estimating joint roughness coefficients", Paper presented at the International journal of rock mechanics and mining sciences & geomechanics abstracts.

Usol'tseva, O.M., Tsoi, P.A. and Semenov, V.N. (2020), "Experimental study of shear behavior of rock joints under two types of boundary conditions: Constant normal load and constant normal stiffness", *IOP Conf. Ser.: Earth Environ. Sci.*, **459**(4), 042019. https://doi.org/10.1088/1755-1315/459/4/042019.

Verma, H., Ray, A., Rai, R., Manna, B. and Singh, T.N. (2023), "Numerical analysis of a tunnel passing through jointed rockmass", *J. Geol. Soc. India*, **99**(12), 1683-1694. https://doi.org/10.1007/s12594-023-2524-5.

Wang, P., Liu, Z., Cai, M. and Labuz, J.F. (2022), "Shear behavior of synthetic rough jointed rock mass with 3d-printed jointing", *Arab. J. Geosci.*, **15**(5), 392-392. https://doi.org/10.1007/s12517-022-09706-y.

Wang, Y., Yang, X., Li, W. and Qiao, W. (2023), "Experimental study on the effect of anchored bolts on failure and strength behavior of nonpersistent jointed rock model", *Bull. Eng. Geol. Environ.*, **82**(3), https://doi.org/10.1007/s10064-023-03129-z.

Wang, X., Yuan, W., Yan, Y. and Zhang, X. (2020), "Scale effect of mechanical properties of jointed rock mass: A numerical study based on particle flow code ", *Geomech. Eng.*, **21**(3), 259-268. https://doi.org/10.12989/gae.2020.21.3.259.

Wu, J., Liu, J. and Son, Y. (2022), "Numerical simulation of the dilatation characteristics of rock joints under constant normal stiffness boundary conditions", *J. Min. Strata Control Eng.*, **4**(2), 71-81. https://doi.org/10.13532/j.jmsce.cn10-1638/td.20211211.001.

Wu, X., Zheng, H., Jiang, Y., Deng, T., Xiao, G. and Wang, Y. (2022), "Effect of cyclic shear loading on shear performance of rock bolt under different joint roughness", *Rock Mech. Rock*

Eng., **56**(3), 1969-1980. https://doi.org/10.1007/s00603-022-03174-2.

Zhang, S., Zheng, X., Wang, C. and Wang, G. (2023), "Shear behavior and asperity damage of 3d rough joints under cns boundary conditions based on czm simulation ", *Sustainability*, **15**(6), 5064. https://doi.org/10.3390/su15065064.

Zhu, L., Wang, L., Zheng, L., Xie, N., Wang, C., Sun, Z., Wang, C. Wu, S. and Fan, B. (2023), "Shear creep characteristics and creep constitutive model of bolted rock joints", *Eng. Geol.*, **327**, 107368-107368. https://doi.org/10.1016/j.enggeo.2023.107368.

Zou, J. and Zhang, P. (2021), "A semi-analytical model of fully grouted bolts in jointed rock masses", *Appl. Math. Model.*, **98**(prepublish), 266-286. https://doi.org/10.1016/j.apm.2021.05.012.

GC